Feasibility Study on the Use of Slag Aggregates in Bio-Shielding Concrete Based on McCARD Radiation Shielding and Activation Analyses

Ikje Noh [a], JinSu Kang [b], SangHyeon Cheong [b], WooJae Kim [b], Hyung Jin Shim [a*]
[a]*Seoul National University, Seoul 08826, Republic of Korea*
[b]*R&D Center, POSCO E&C, Incheon 22009, Republic of Korea*
[*]*Corresponding author: shimhj@snu.ac.kr*

***Keywords :** slag aggregate, bio-shielding concrete, radiation shielding, activation, McCARD

1. Introduction

Nuclear power is attracting renewed attention worldwide as a reliable low-carbon energy source for achieving net zero [1]. Nevertheless, the introduction and expansion of nuclear power continue to be constrained by the capital cost burden of new builds. As one of the measures to relieve this cost burden, the adoption of functionalized concrete, which improves specific properties of concrete at low cost, has been proposed for new nuclear power plants (NPPs) [2]. In line with this approach, this study focuses on the use of industrial by-product slag as a concrete aggregate. Replacing natural aggregates, whose prices are expected to rise as their reserves are depleted and their extraction is increasingly restricted [3], with less expensive industrial by-product slags can reduce the material cost of concrete. This substitution also implies environmental benefits, in that it recycles industrial by-products and reduces the consumption of natural aggregates.

Meanwhile, the mechanical properties and durability of concretes incorporating slag aggregates have been studied for conventional construction applications [4–6], and the relevant Korean industrial standards for slag aggregates have been established [7]. For application to NPPs, however, additional requirements must be satisfied. In particular, the bio-shielding concrete surrounding the reactor core must satisfy the radiation shielding performance criteria. In addition, if the bio-shielding concrete becomes more activated than conventional concrete, the resulting increase in radioactive waste disposal cost could negate the economic benefit of the slag aggregates. In this study, therefore, the feasibility of slag-incorporated concrete for NPPs is examined by evaluating its shielding performance and activation level as the bio-shielding concrete.

2. Analysis Scope and Methods

This section first defines the analysis scope, which covers the candidate industrial by-product slags and the compositions of the slag-incorporated concretes, and then describes the analysis methods, including the simplified analysis model and the neutron and photon source terms for the shielding and activation analyses.

2.1 Candidate Slags and Concrete Compositions

Three candidate industrial by-product slags for NPP shielding concrete were selected: blast furnace slag (BFS), ferronickel slag (FNS), and copper smelting slag (CSS). According to the relevant Korean industrial standards [7], BFS is applicable as fine aggregate, coarse aggregate, and mineral admixture, whereas FNS and CSS are applicable as fine aggregate. Since BFS admixture is already in use in NPP concrete [8], the scope of this study was limited to the application of the slags as fine aggregates. Although electric arc furnace oxidizing slag is also permitted as a concrete aggregate by the Korean industrial standards [7], it was excluded because its use is restricted by the risk of expansive disintegration of concrete caused by its free CaO content [9]. Lead slag, which is likewise applicable as a concrete aggregate [7], was also excluded because its generation is far smaller than those of the other candidate slags.

For Fe, Co, and Eu, which are expected to dominate the shielding and activation behavior [10], inductively coupled plasma (ICP) analyses were performed on three samples of each candidate slag, and the averaged values were adopted. The compositions of the other elements were taken from the literature [11], and the composition of the reference fine aggregate used in the bio-shielding concrete of existing NPPs was taken from NUREG/CR-3474 [12]. The densities and material compositions of the reference aggregate and the three candidate slags are summarized in Table I.

Table I: Density and material compositions of the reference aggregate and the candidate slags

Item	Ref.	BFS	FNS	CSS
Density [g/cm³]	2.60	2.58	2.95	3.54
Si [wt%]	12.81	16.41	24.28	18.28
Ca [wt%]	24.28	31.16	1.96	3.56
Na [wt%]	0.75	0.00	0.00	0.00
Al [wt%]	2.79	7.77	1.09	2.89
S [wt%]	0.17	0.93	0.04	0.91
K [wt%]	0.93	0.00	0.00	0.00
Fe [wt%]	1.64	0.30	9.99	37.67
O [wt%]	56.63	40.28	43.46	35.32
Mg [wt%]	0.00	3.16	19.17	1.36
Co [ppm]	5.89	1.09	79.8	155.7
Eu [ppm]	0.55	3.68	0.00	0.40

Using the reference fine aggregate and the three candidate slags, four concrete compositions were considered in the analysis. Case 1 uses only the reference fine aggregate, with a concrete density of 2.30 g/cm³. In Cases 2, 3, and 4, the reference fine aggregate is replaced by BFS, FNS, and CSS, respectively; the resulting concrete densities are 2.29, 2.41, and 2.58 g/cm³. In deriving the concrete compositions and densities, the following assumptions were made: (a) all constituents of the concrete other than the fine aggregate, including cement, water, and the coarse aggregate, are taken from Ref. [12] and applied identically to all cases; (b) in Case 1, the total mass of the fine and coarse aggregates accounts for 73.4% of the concrete mass [12], and the mass ratio of fine to coarse aggregate is 1:1, as is typical in concrete mixing; (c) in Cases 2, 3, and 4, the reference fine aggregate is replaced by an equal volume of slag aggregate; (d) among the trace elements of the reference aggregate, only Co and Eu are assigned to the aggregate composition; (e) natural isotopic abundances are applied to all elements; (f) in all cases, the concrete is modeled as a homogeneous mixture of its constituent elements; and (g) reinforcing steel is not considered.

2.2 Shielding and Activation Analysis Model

Since the objective of this study is to confirm the feasibility of the slag aggregates, a simplified one-dimensional slab model was adopted. In the slab model, the neutron and photon transport and depletion calculations were performed with McCARD [13, 14]. The 200-cm-thick concrete slab, divided into forty 5-cm-thick segments, is irradiated on one side by the radiation source term, with void regions on both sides and reflective boundary conditions imposed on the lateral surfaces, as illustrated in Fig. 1. The activation of the concrete was evaluated from the nuclide inventory of each concrete segment as a function of irradiation and cooling time.

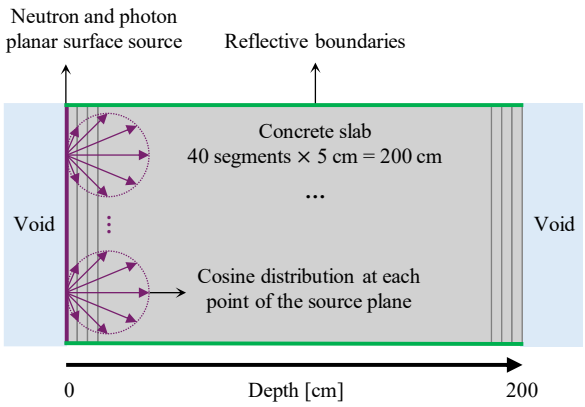


Fig. 1. One-dimensional slab model for the shielding and activation analyses.

The source term applied to the slab model was derived from a full-core calculation of Kori Unit 1 performed with McCARD. Kori Unit 1 was selected because information on its constituent material, geometry, and operation history is available and its decommissioning schedule has been finalized [15], which enables realistic shielding and activation analyses. Considering that the accumulation of long-lived radioactive products in concrete is proportional to the total neutron fluence over a given period, representative burnup points were selected instead of simulating the entire operation history, which is computationally prohibitive. Since the neutron flux varies considerably over the early cycles and reaches an equilibrium after a certain cycle, the operation history was divided into a non-equilibrium period, Cycles 1–11 (3,473 EFPD), and an equilibrium period, Cycles 12–32 (7,501 EFPD), and one representative burnup point was selected for each period. For each period, the burnup point whose neutron flux is closest to the period-averaged value was adopted as the representative burnup point, i.e., the middle of cycle (MOC) of Cycle 5 and Cycle 29 [16]. In addition, the reactor was assumed to operate continuously at full power over each period, and the shutdown periods were not considered. In both the Kori Unit 1 full-core calculation and the slab-model calculations, Cooper's weight window method [17] was applied as a variance reduction technique, and the relative statistical uncertainties of the calculated fluxes were thereby kept below 1%.

From the axial distribution of the calculated neutron flux in the bio-shielding concrete, the concrete within ±15 cm of the active core mid-plane was chosen as the representative position, where a relatively high degree of activation is expected. The radiation source term applied to the slab model was modeled as a planar surface source on the inner face of the concrete slab, whose magnitude was normalized to the inward partial current of particles entering the concrete surface tallied at the representative position in the full-core calculation. In the slab model, source directions were sampled from a cosine distribution over the inward 2π solid angle, as depicted in Fig. 1, corresponding to an isotropic angular flux incident on the concrete surface. This treatment is supported by the full-core calculation, in which the ratio of the inward partial current to the inward flux at the concrete surface was approximately 0.5, indicating that the incident angular flux is nearly isotropic. The cosine distribution, however, was applied uniformly over all energy groups, and the energy dependence of the incident angular distribution was thus neglected.

The neutron source intensities of the slab model, expressed as the corresponding inward neutron flux, are 2.07×10^{10} and 1.41×10^{10} [$cm^{-2}\cdot s^{-1}$] at Cycle 5 MOC and Cycle 29 MOC, respectively. The neutron energy spectra of the slab-model source are shown in Fig. 2; they were tallied in 95 energy groups at the two representative burnup points. Since the difference between the two spectra is small, the Cycle 29 MOC spectrum was applied to both the shielding and the activation analyses, and the difference between the two periods was represented by the source intensity.

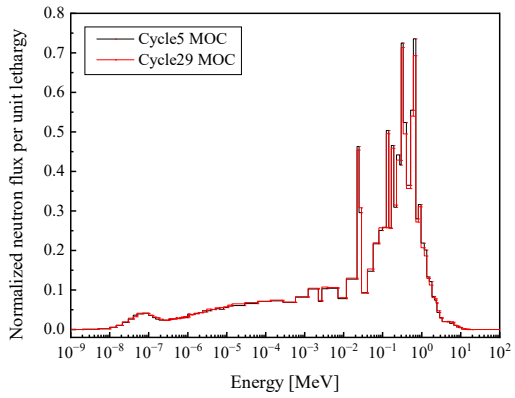


Fig. 2. Energy spectra of the neutron source applied to the slab model.

The photon source applied to the shielding analysis comprises prompt fission gammas together with capture and inelastic-scattering gammas generated by neutron transport; gammas from fission-product decay are not included. As in the neutron shielding analysis, the photon energy spectrum at Cycle 29 MOC was applied as the slab-model source for the photon shielding analysis; it was tallied in 25 energy groups and is shown in Fig. 3. The photon source intensity of the slab model, expressed as the corresponding inward photon flux, is 4.07×10^{9} [$cm^{-2}\cdot s^{-1}$] at Cycle 29 MOC. In this analysis, the primary photons were transported from this surface source, while the secondary photons generated by neutron capture and inelastic scattering within the concrete were obtained from the coupled neutron–photon transport of the neutron source. Delayed photons from activation nuclides in the concrete were not considered.

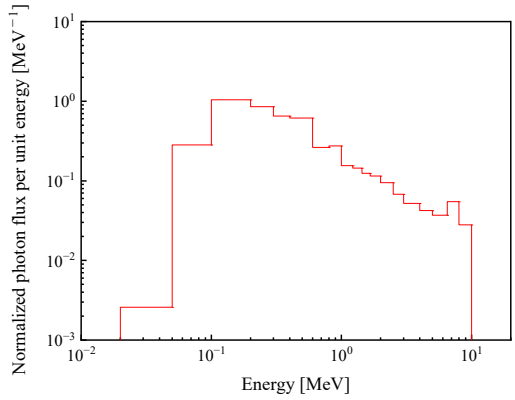


Fig. 3. Energy spectrum of the photon source applied to the slab model.

3. Results

3.1 Radiation Shielding Performance

Fig. 4 compares the depth profiles of the neutron and photon fluxes for the four cases, together with the relative differences from the reference (Case 1). After a build-up region within the first 10–15 cm, where the hard incident spectrum is thermalized, all components attenuate nearly exponentially with depth. For the neutron flux, the FNS and CSS concretes attenuate more strongly than the reference, and the accumulated reduction grows with depth, reaching 69% and 82%, respectively, at the outer surface. In contrast, the BFS concrete remains within ±15% of the reference over the entire depth, providing no meaningful improvement. The primary photon flux shows the same trend — reductions of about 40% for FNS and 81% for CSS at the outer surface — reflecting the higher densities of these concretes, and the secondary photon flux also behaves similarly beyond the first few segments.

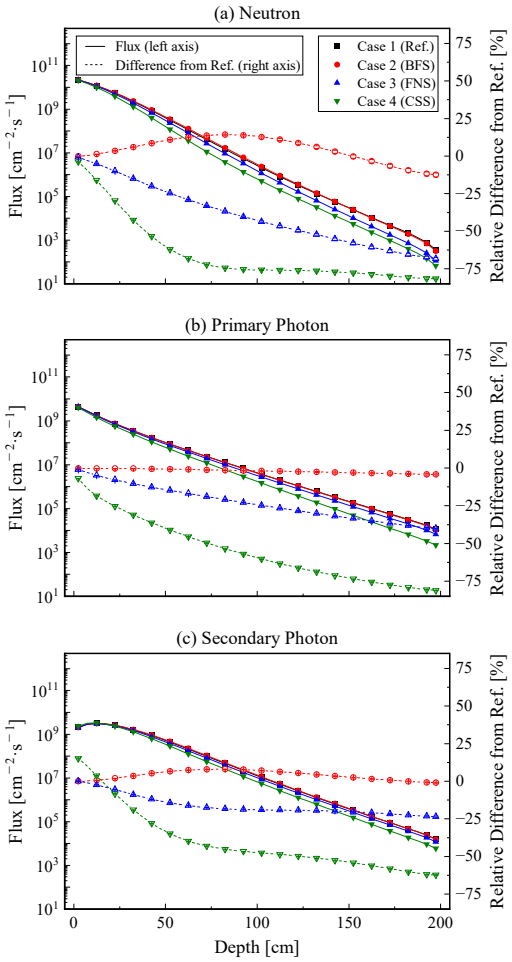


Fig. 4. Depth profiles of (a) the total neutron flux, (b) the primary photon flux, and (c) the secondary photon flux in the concrete shield for the four cases, together with the relative difference of each case from Case 1 (right axis, open symbols).

Fig. 5 further decomposes the neutron flux into the thermal, epithermal, and fast groups. As shown in Fig. 5(a), the thermal flux of the Fe-rich CSS concrete is progressively suppressed by the strong thermal-neutron absorption of Fe, with the relative difference from the reference growing to about −65% within the first 50 cm. Since the thermal and epithermal groups dominate the flux magnitude, the behavior of the total flux largely follows theirs. In the epithermal and fast groups, on the other hand, the FNS and CSS concretes attenuate the flux

at nearly the same rate, as shown in Figs. 5(b) and 5(c): at the outer surface, the epithermal flux is reduced by 69% and 72% and the fast flux by 73% and 77% for FNS and CSS, respectively — a difference of less than 4 percentage points. The two concretes thus provide comparable shielding performance for the fast group, which dominates the neutron dose owing to its much larger flux-to-dose conversion coefficients.

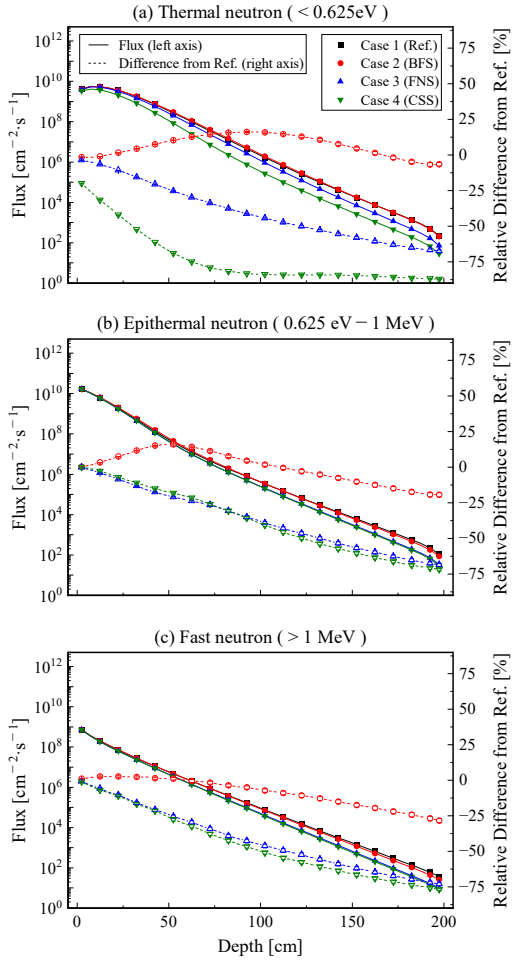


Fig. 5. Depth profiles of (a) the thermal (< 0.625 eV), (b) the epithermal (0.625 eV – 1 MeV), and (c) the fast (> 1 MeV) neutron fluxes in the concrete shield for the four cases, together with the relative difference of each case from Case 1 (right axis, open symbols).

Since the flux profiles are not strictly exponential — the local attenuation coefficient is small in the near-surface build-up region, increases as the incident spectrum is thermalized, and then decreases gradually — a single attenuation coefficient fitted over the whole depth depends on the choice of the fitting range. Therefore, interval-averaged linear attenuation coefficients, defined in Eq. (1), were instead evaluated for three depth intervals, from the segment-averaged fluxes of the two segments bounding each interval, as listed in Table II.

$$\overline{\mu} = \frac{\ln[\phi(x_a)/\phi(x_b)]}{x_b - x_a} \qquad (1)$$

where $\phi(x_a)$ and $\phi(x_b)$ are the segment-averaged fluxes of the segments located at x_a and x_b bounding each depth interval.

For the neutron flux, the advantage of CSS is concentrated in the first interval, where its $\overline{\mu}$ exceeds that of the reference by 22%, but diminishes to about 5% in the deepest interval, whereas FNS maintains a nearly uniform improvement of 6–7% over the entire depth; the BFS coefficients remain within about 3% of the reference in all intervals, consistent with the sign reversal of its relative difference in Fig. 4(a). For the primary photons, the improvement follows the concrete density in all intervals, with CSS exceeding the reference by 12% on average.

Table II: Interval-averaged linear attenuation coefficients $\bar{\mu}$ [cm^{-1}] of the neutron and primary photon fluxes

Case	0–50 cm	50–150 cm	150–200 cm
Neutron			
Case 1 (Ref.)	0.0830	0.0955	0.0927
Case 2 (BFS)	0.0809	0.0963	0.0957
Case 3 (FNS)	0.0885	0.1013	0.0990
Case 4 (CSS)	0.1015	0.1016	0.0969
Primary photon			
Case 1 (Ref.)	0.0797	0.0621	0.0616
Case 2 (BFS)	0.0798	0.0623	0.0619
Case 3 (FNS)	0.0827	0.0646	0.0640
Case 4 (CSS)	0.0890	0.0701	0.0692

3.2 Activation and Radioactive Waste Classification

Based on the depletion calculations of the slab model performed with McCARD, the nuclide-wise specific activity of each 5-cm concrete segment was evaluated as a function of cooling time. Considering only the activation products, each segment was then classified into intermediate-level waste (ILW), low-level waste (LLW), very-low-level waste (VLLW), and clearance waste according to the nuclide-wise concentration limits and the sum-of-fractions (SOF) criterion of the Korean radioactive waste classification regulation [18].

Table III lists the maximum depth and the volume fraction of each waste level at a cooling time of 20 years, consistent with the planned dismantling schedule of Kori Unit 1 [15], and Fig. 6 shows the boundary depths as functions of cooling time. Each boundary depth was determined by log-linear interpolation of the SOF profile between the two adjacent segments, and its 1σ statistical uncertainty was evaluated from the relative standard deviations of the two segment activities bracketing the boundary, taken as those of the corresponding segment-wise thermal neutron fluxes. The resulting uncertainties are below 0.2 cm in all cases, smaller than the plotted symbols. Note that the quoted uncertainties include only the Monte Carlo statistical uncertainties; systematic uncertainties, such as those in the aggregate compositions, the source-term modeling assumptions, and the nuclear data, are not included.

Since the specific activity of each activation product is proportional to the content of its parent element, the sensitivity of the boundary depths to the Co and Eu contents can be estimated from the log-slope of the SOF profile. Because the SOF decreases nearly exponentially with depth, the boundary depths respond only logarithmically to the impurity contents: a ±20% change in the Eu content moves the boundaries by at most 2.0 cm (BFS), and the same change in the Co content by at most 1.2 cm (CSS) — far smaller than the differences between the cases — so the case ranking is robust against variations of this magnitude in the impurity contents. In the resulting classification, no segment exceeded the ILW criteria at any time after shutdown. At the 20-year cooling time, the clearable fraction of the wall ranges from 23.6% for BFS to 36.4% for CSS. After a sharp retreat during the first year of cooling caused by the decay of short-lived nuclides, the boundaries recede only slowly thereafter.

Table III: Maximum depth and volume fraction of each waste level in the 200-cm shield wall at a cooling time of 20 years

Case	Maximum Depth [cm] (Volume Fraction)		
	LLW	VLLW	Clearance
Case 1 (Ref.)	91.60 ± 0.01 (45.8%)	140.20 ± 0.03 (24.3%)	200 (29.9%)
Case 2 (BFS)	103.64 ± 0.05 (51.8%)	152.79 ± 0.16 (24.6%)	200 (23.6%)
Case 3 (FNS)	86.65 ± 0.04 (43.3%)	132.10 ± 0.13 (22.7%)	200 (34.0%)
Case 4 (CSS)	81.32 ± 0.04 (40.6%)	127.16 ± 0.16 (23.0%)	200 (36.4%)
Note: The ± values denote the 1σ statistical uncertainties.			

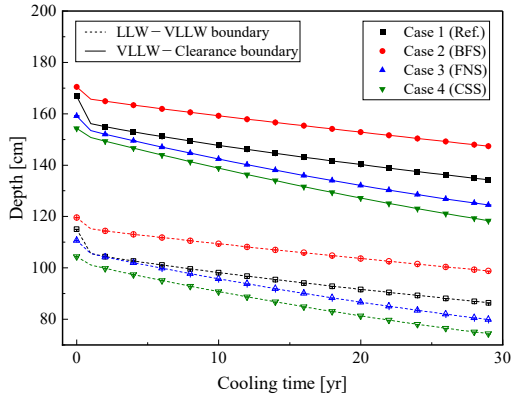


Fig. 6. Waste-level boundary depths as functions of cooling time for the four cases.

Fig. 7 presents the depth profiles of C_i/L_i – the ratio of the specific activity of each nuclide to its concentration limit in the regulation [18] — for the five dominant contributors. These five nuclides together account for more than 99.9% of the SOF in all cases. In Cases 1 and 2, Eu-152 governs the classification, whereas in the Fe-rich Cases 3 and 4 the Co-60 contribution becomes comparable to or exceeds that of Eu-152, showing that the dominant nuclide governing the waste level itself depends on the aggregate impurities. Note that the boundaries are determined by the SOF, not by any individual ratio.

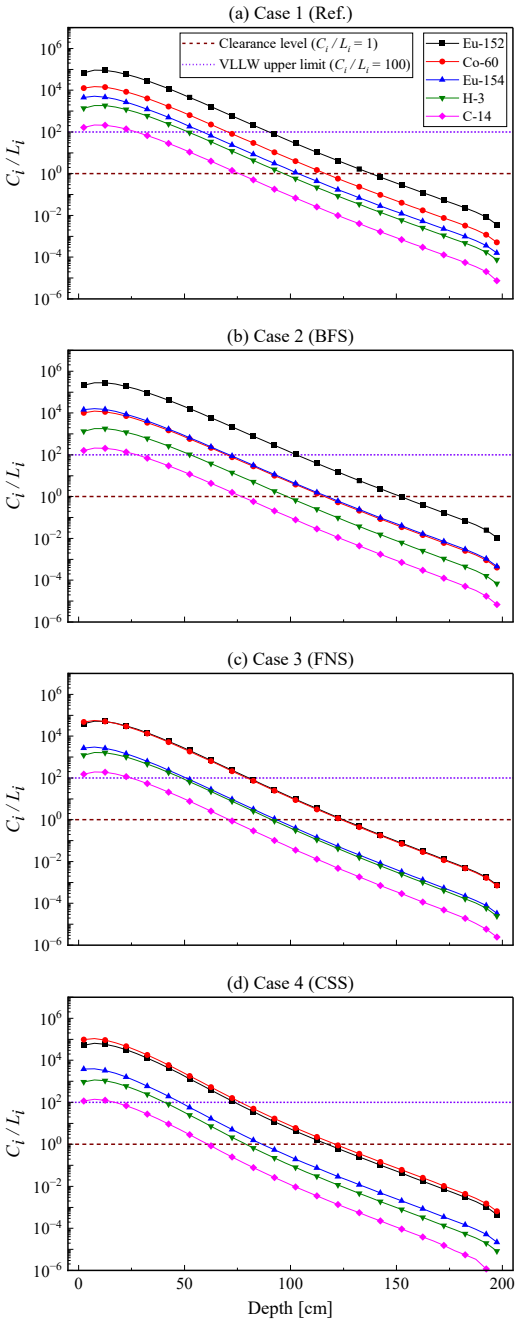


Fig. 7. Depth profiles of the concentration-to-limit ratio C_i/L_i of the five dominant nuclides at a cooling time of 20 years for (a) Case 1, (b) Case 2, (c) Case 3, and (d) Case 4.

4. Conclusions

The radiation shielding performance and the activation characteristics of bio-shielding concretes incorporating BFS, FNS, and CSS fine aggregates were evaluated with McCARD slab-model calculations driven by a Kori Unit 1 full-core source term, and the concrete of each case was classified according to the Korean radioactive waste classification regulation. The main conclusions are as

follows. First, the FNS and CSS concretes provide clearly enhanced neutron and photon shielding owing to their higher densities, whereas the BFS concrete shows no improvement over the reference. In particular, the neutron shielding improvement of CSS is most pronounced in the thermal group owing to the strong thermal-neutron absorption of Fe, while FNS and CSS attenuate the fast group, which dominates the neutron dose, at nearly the same rate. Second, the waste classification is governed by Eu-152 and Co-60 — the impurities identified as dominant in previous studies [10] and accordingly the only trace elements considered in this analysis — while the dominant nuclide between the two changes with the aggregate impurities. At the 20-year cooling time, the Eu-rich BFS deepens the waste boundaries beyond those of the reference despite its comparable shielding performance. In contrast, CSS yields the shallowest boundaries, as its strong suppression of the thermal flux, which governs the activation, outweighs its high Co content, and FNS is favorable in both respects.

Several limitations should be noted. First, this study compared the slag concretes with the reference concrete at the position where the highest activation is expected, and therefore does not quantify the actual activation level or the resulting change in the total radioactive waste inventory of an NPP. Second, the transportation distance from the slag production sites — a major component of the aggregate cost, which may weigh more heavily on the high-density CSS — was not considered in the discussion of the economic feasibility of the slag aggregates. Third, the compositional variability of the slag and reference aggregates with their sources and production times was not addressed.

Within this scope, the analyses confirm the feasibility of the slag fine aggregates for bio-shielding concrete: FNS is favorable in both shielding and waste generation; CSS provides the largest gains if the transportation burden is acceptable; whereas BFS offers no clear advantage over the reference aggregate. In addition, evaluations of the mechanical properties and durability, together with long-term irradiation tests, are required for actual NPP applications. Shielding and activation analyses based on a full simulation of an NPP employing the slag aggregates, together with an economic feasibility assessment based on their results, would also be necessary.

Acknowledgements

This work was supported by POSCO E&C Co., Ltd. (Contract No. 2025-T-W-1006).

REFERENCES

[1] R. M. Grossi, The Time is Now: Nuclear for a Net Zero Future, IAEA Bulletin, Vol.65, No.3, International Atomic Energy Agency, Vienna, 2024.
[2] MIT Energy Initiative, The Future of Nuclear Energy in a Carbon-Constrained World, Massachusetts Institute of Technology, Cambridge, MA, 2018.
[3] Ministry of Land, Infrastructure and Transport, 2026 Aggregate Supply Plan (in Korean), Sejong, Republic of Korea, 2026.
[4] R. K. Patra and B. B. Mukharjee, Influence of Incorporation of Granulated Blast Furnace Slag as Replacement of Fine Aggregate on Properties of Concrete, Journal of Cleaner Production, Vol.165, p.468, 2017.
[5] J. Sun, J. Feng, and Z. Chen, Effect of Ferronickel Slag as Fine Aggregate on Properties of Concrete, Construction and Building Materials, Vol.206, p.201, 2019.
[6] B. H. J. Pushpakumara and P. M. K. N. Bandara, Evaluating the Effectiveness of Copper Slag Waste as a Fine Aggregate in Concrete, Construction and Building Materials, Vol.475, 141046, 2025.
[7] KS F 2527, Concrete Aggregates, Korean Standards Association.
[8] J. M. Noh, Concrete Mix Proportion and Slump for Export of Nuclear Power Plants, Magazine of the Korea Concrete Institute, Vol.36, No.5, p.46, 2024.
[9] T. B. Min, H. Y. Kim, and H. S. Lim, Characteristics of Electric Arc Furnace Oxidized Slag and Domestic and International Research Trend, Magazine of RCR, Vol.14, No.2, p.40, 2019.
[10] B. Babcsany, S. Czifrus, and S. Feher, Methodology and Results of Activation Calculation of a VVER-440 Nuclear Power Plant, Nuclear Engineering and Design, Vol.284, p.228, 2015.
[11] S. K. Seo and J. H. Choi, Characteristics and Utilization of Slag Aggregates, Magazine of the Korea Concrete Institute, Vol.13, No.1, p.66, 2001.
[12] J. C. Evans, E. L. Lepel, R. W. Sanders, C. L. Wilkerson, W. Silker, C. W. Thomas, K. H. Abel, and D. R. Robertson, Long-Lived Activation Products in Reactor Materials, NUREG/CR-3474, Pacific Northwest Laboratory, Richland, WA, 1984.
[13] H. J. Shim, B. S. Han, J. S. Jung, H. J. Park, and C. H. Kim, McCARD: Monte Carlo Code for Advanced Reactor Design and Analysis, Nuclear Engineering and Technology, Vol.44, p.161, 2012.
[14] D. H. Lee and H. J. Shim, Verification of McCARD Radiation Shielding Analysis Capability Using the SINBAD Database, Transactions of the Korean Nuclear Society Meeting, 2018.
[15] Korea Hydro & Nuclear Power Co., Final Decommissioning Plan for Kori Unit 1, 2021.
[16] Y. Kim, S. Jang, D. Lee, and H. J. Shim, Validation of Activation Analysis Method on RV/RVI of Kori Unit 1 Using McCARD/ORIGEN2, Proceedings of the Reactor Physics Asia Conference 2019 (RPHA19), 2019.
[17] M. A. Cooper and E. W. Larsen, Automated Weight Windows for Global Monte Carlo Particle Transport Calculations, Nuclear Science and Engineering, Vol.137, No.1, p.1, 2001.
[18] Nuclear Safety and Security Commission, Notice No. 2025-11, Regulations on Classification of Radioactive Waste and Criteria for Self-Disposal, 2025.